

Article

Mechanical Measurement Approach to Characterize Venting Behavior during Thermal Runaway of 18650 Format Lithium-Ion Batteries

Elisabeth Irene Gillich , Marco Steinhardt , Yaroslava Fedoryshyna  and Andreas Jossen 

Chair of Electrical Energy Storage Technology, Department of Energy and Process Engineering, School of Engineering and Design, Technical University of Munich, Arcisstraße 21, 80333 Munich, Germany

* Correspondence: elisabeth.gillich@tum.de

Abstract: The propagation of thermal runaway in a battery system is safety-critical in almost every application, such as electric vehicles or home storage. Abuse models can help to understand propagation mechanisms and assist in designing safe battery systems, but need to be well-parametrized. Most of the heat during thermal runaway is released by venting that is why the characteristic of the vent flow plays an important part in the safety assessment. During venting, the cell generates a recoil force like a rocket, which depends on the flow speed and flow rate of the gas. This principle is used in this work to measure the velocity and mass flow rate of the vent gas. High-power and high-energy 18650 format lithium-ion batteries were overheated and the recoil and weight forces were measured to determine the venting parameter during thermal runaway. Our results show, that the linearized gas flow rate for the high-power and high-energy cell is 22.15 gs^{-1} and 27.92 gs^{-1} , respectively. The progress of the gas velocity differs between the two cell types and in case of the high-energy cell, it follows a single peak asymmetrical pattern with a peak of 398.5 ms^{-1} , while the high-power cell shows a bumpy pattern with a maximum gas velocity of 260.9 ms^{-1} . The developed test bench and gained results can contribute insights in the venting behavior, characterize venting, support safety assessments, simulations and pack design studies.

Keywords: lithium-ion battery; thermal runaway; mass loss; venting; gas velocity; gas flow rate; recoil force



Citation: Gillich, E.I.; Steinhardt, M.; Fedoryshyna, Y.; Jossen, A. Mechanical Measurement Approach to Characterize Venting Behavior during Thermal Runaway of 18650 Format Lithium-Ion Batteries. *Batteries* **2024**, *10*, 142. <https://doi.org/10.3390/batteries10040142>

Academic Editor: Wojciech Mrozik

Received: 12 March 2024

Revised: 17 April 2024

Accepted: 20 April 2024

Published: 22 April 2024



Copyright: © 2024 by the authors. Licensee MDPI, Basel, Switzerland. This article is an open access article distributed under the terms and conditions of the Creative Commons Attribution (CC BY) license (<https://creativecommons.org/licenses/by/4.0/>).

1. Introduction

Lithium-ion batteries (LIBs) are the state-of-the-art energy storage technology for mobile and consumer applications. In this context, high performance and long service life are just as important as product safety. Production errors or exposure of LIBs to conditions beyond their operating range may lead to an exothermic chain reaction called thermal runaway (TR). During TR, the electrodes, separator and electrolyte are decomposed, releasing gas and heat. To avoid uncontrolled rupture and explosion, cylindrical cells are usually equipped with a safety valve in the top cap, which opens at a critical pressure. Generated gas, liquids and solid particles are ejected, which not only lowers internal pressure but also releases a significant amount of heat [1–3].

While this helps to cool down the failed cell, the ejecta may increase the heat transfer to adjacent cells e.g., in a battery module and trigger them into TR. Thermal runaway propagation (TRP) can lead to catastrophic failures of entire battery systems, which is why the corresponding heat pathways are of high interest in battery safety research as well as battery development and system design.

Several studies use different types of calorimeters to quantify the heat generation during TR [1,4–6] and the combustion energetics of ejected materials [7–9]. Wang et al. [10] and Ren et al. [11] use similar calorimetric methods to understand how cell aging influences

the TR behavior. Their main finding is that lithium plating decays thermal stability, while other aging effects does not affect or even improve the TR performance.

Besides the calorimetric studies, some approaches take a closer look at gas generation and gas venting as part of the TR. Finegan et al. [12–14], Kong et al. [15] and Yao et al. [16] use computer tomography to visualize the TR processes inside the battery cell. This method allows identifying where the material decomposition starts and how it propagates through the battery cell. In the work of Golubkov et al. [17], Lammer et al. [4] and Sturk et al. [18], the vented gas is analysed using gas chromatography to identify its components. Essl et al. [19] and Cai et al. [20] use the occurrence of certain gases and integrate gas sensors in the battery to detect TR at an early stage.

Mier et al. [21] employ Schlieren Imaging to visualize the vent flow during abuse testing. The consecutive study [22] focuses on the fluid flow through the vent cap and identifies key parameters of a simulated vent flow, such as burst pressure, opening area and discharge coefficient.

In addition to the experimental studies presented above, there are also numerous simulative approaches to model TR and venting. One of the first thermal abuse models was published by Hatchard et al. [23]. The model considers the three decomposition reactions to simulate the thermal behavior: solid-electrolyte interphase (SEI) decomposition, decomposition of anode and electrolyte, and cathode decomposition. Kim et al. [24] considered additional reactions in a 3D abuse model for large-format cells and simulated the propagation inside the cell. They simulated oven test and a localized heat release to show the different thermal cell responses. The location of TR initiation might be of interest, then with the empirical model from Finegan et al. [5], the dependency between cell surface temperature and location of initiated TR can be investigated. The TR models mentioned so far base on conductive heat transfers and neglect venting. However, Hoelle et al. [25] showed with an 3D empirical computational fluid dynamics (CFD) model that it is necessary to consider the mass loss through venting during TR.

Rising cell temperatures cause an increase in decomposition reactions, which generates gas inside the cell. When the cell pressure reaches the burst pressure of the safety valve, venting occurs and leads to a change of cell mass. Coman et al. presented a model [26] of an 18650 cylindrical cell which considers the influence of electrolyte evaporation and venting on the temperature and pressure behavior of the cell. In a further study [27] they implemented gas generation from the SEI decomposition reaction, which led to a better time response of the venting.

With thermal abuse models it is possible to simulate the cell behavior up to the opening of the safety valve, which can be used to design early warning system with gas sensors in battery packs [28]. Ostanek et al. [29] developed a coupled thermal and venting model to simulate the cell temperature response and gain details on the progression of TR. They also used the model to investigate the influence of cell design parameters regarding the time on appearance of venting and TR.

The venting of gases from a single LIB during an abuse process has a major impact on the TRP within a battery system [30]. Therefore, some studies enhanced the TR modeling by flow field simulations to model the vent behavior outside the cell [30–35]. A few models considered the ignition of the vent and investigated the jet flame without [33] and with the impact of particles [34,35]. They all determined the properties of ejected gases based on pressure behavior of an ideal gas and a given gas composition. Therefore, the venting properties such as mass flow rate, vent velocity and venting temperature are the coupling parameters between the thermal abuse model of a single cell and the flow model outside the cell. When investigating the TRP within a battery system, the computational effort can be reduced by looking only at the flow model outside the cell if the venting parameters are available or empirically determined. Mishra et al. [36] presented such a model and investigated the impact of battery pack design parameters on the TRP. They used measured stagnation pressure and mass flow rates [22] to determine the input model parameters vent gas velocity and temperature as a function of time.

Table 1 lists experimental studies on venting parameters during TR of a LIB triggered by overheating. The table is sorted by the methodology and gives an overview of the research on mass flow rate and vent flow velocity. The parameter vent temperature is not listed, because it is studied in a wide range [3,8,37–40] and usually measured by placing a thermocouple in front of the vent area. Most of the work has been published by the State Key Laboratory of Fire Science from the University of Science and Technology of China [38,41–47]. The first venting is given by the opening of the safety valve due to a critical cell pressure. Thereafter, the TR event occurs which involves a skyrocketing temperature behavior.

Table 1. A summary of experimental research on mass flow rate and vent flow velocity during thermal runaway of lithium-ion batteries. Only experiments with overheating as a trigger method are considered.

Ref.	Methodology	Cell Format	Cathode Chemistry and Nominal Capacity	Mass Flow Rate	Vent Flow Velocity	Comment
[41]	weight sensor	prismatic	LFP: 27 Ah	✓	✓	Assuming ideal gas flow and a given gas composition
[42]	weight sensor	prismatic	LFP: 86 Ah	✓		
[46]	weight sensor	prismatic	LFP: 280 Ah	✓		
[38]	weight sensor, optical	prismatic	NMC ₁₁₁ : 38 Ah		✓	High-speed camera
[34]	weight sensor, pitot tube	prismatic	LFP: 27 Ah	✓	✓	
[43,45]	weight sensor, pitot tube	prismatic	LFP: 32 × 86 Ah (pack) LFP: 100 Ah	✓	✓	Assuming ideal gas flow and a given gas composition
[28]	weight sensor, pressure sensor	21700	NCA	✓		Only data during opening of safety valve available
[48]	weight sensor, pressure sensor	pouch	NMC ₈₁₁ : 124 Ah (pack)	✓	✓	Assuming isotropic and ideal gas flow
[49–51]	optical	18650	NMC ₆₂₂ : 2.0 Ah LFP: 1.8 Ah LCO: 2.6 Ah		✓	Schlieren technique and Natural Luminosity, in [51] additionally OH*-chemiluminescence
[47]	momentum and mass conservation	prismatic	NMC ₇₁₂ : 52 Ah	✓	✓	6-axis mechanical sensor, measuring frequency 40 Hz, evaluated frequency 1 Hz
This work	momentum and mass conservation	18650	NMC ₈₁₁ : 3.5 Ah NCA: 2.5 Ah	✓	✓	3-axis force sensor, measuring frequency 10 kHz, evaluated frequency 100 Hz

A common method to determine the mass flow rate is via the change of cell mass. For that, electronic mass balances or weight sensors are used and placed underneath the LIB during the thermal abuse tests [28,41–43,45,46].

Prismatic lithium-iron-phosphate (LFP) LIBs with a capacity from 86 Ah up to 280 Ah were reported with a mass flow rate of 20.8 gs⁻¹ up to 180.4 gs⁻¹ for the opening of the safety valve and between 2.7 gs⁻¹ and 22 gs⁻¹ at the TR event [42,43,45,46]. Zhou et al. [41] measured a volume flow rate of 7.51 ls⁻¹ for the first vent and 2.11 ls⁻¹ for the TR event. The research on cylindrical cell formats are rare, but one research published a mass flow rate of 8.51 gs⁻¹ up to 17.01 gs⁻¹ for the opening of the safety valve [28]. Unfortunately, the weight sensor broke at the TR event, thus, only the first venting was characterized. Wang et al. [48] used the ideal gas equation instead of a weight sensor and determined a mass flow rate between 40 gs⁻¹ and 63 gs⁻¹ for a high-energy nickel-cobalt-manganese (NMC) pouch battery pack.

One way to determine the vent flow velocity are optical methods, such as high-speed digital camera [38], Schlieren technique [49–51], Natural Luminosity [49–51] or OH*-chemiluminescence tracking [51]. Zou et al. [38] reported vent velocities at the opening of the safety valve of 40–55 ms⁻¹ and 8.3 ms⁻¹ for the TR event for a 38 Ah prismatic NMC cell. Higher velocities up to 50 ms⁻¹ during the TR event were measured for cylindrical 18650 LIBs [49–51].

Pitot tubes [34,43,45] or pressure sensors [48] are low cost methods to obtain the vent flow velocities. The method principles assumes an ideal gas flow and a given and constant composition of the venting gas. Pitot tubes can be applied only for venting without ignition and is limited to low-density batteries. LFP is such a low-density battery and vent velocities between 19.1 ms⁻¹ to 83.3 ms⁻¹ for a single prismatic cells [43] and 270 ms⁻¹ for a battery pack [45] were obtained at the first venting. At the TR event 14.3 ms⁻¹ [34] up to 24 ms⁻¹ [42] were reported for a single prismatic cell and 36.3 ms⁻¹ for a prismatic battery pack [45], respectively. Results in the same order of magnitude were published for a high-energy pouch battery pack measured by a pressure sensor [48].

Another way to obtain the mass flow rate and vent flow velocity is the momentum and mass conservation method. It was recently published by [47] and has much less requirements on the venting system then the methods with pitot tube or pressure sensors with adiabatic conditions. The momentum and mass conservation method relies on Newton's second and third law. When a LIB undergoes TR with venting, the vent flow induces a force at the vent area and the LIB reacts with an equal opposite force and loses mass at the same time. Li et al. [47] applied this method on a prismatic NMC₇₁₂ cell with 52 Ah. While the venting parameters of prismatic LIBs, especially LFP, was a lot investigated lately, the mass loss rate and gas venting velocity during TR of cylindrical LIBs is not fully elucidated and needs further research.

Our work addresses this gap by developing a test bench based on the momentum and mass conservation method to characterize venting behavior during thermal abuse of cylindrical LIBs. The test bench initiates the TR by overheating and measures the forces that occur during venting with high frequency. Two cell types — a high-power and a high-energy — of the 18650 format are investigated to show the capabilities of the mechanical approach and the test bench. Finally, two sets of parameters of the venting properties of 18650 LIB are presented.

2. Theoretical Approach

The venting behavior during TR of an 18650 format LIB can be compared to the venting of a pressure vessel [52], as shown in Figure 1a,b. Both systems have their contents with the mass m and temperature T in a constant volume V at a pressure p within the cell case and vessel walls, respectively. The mass inside a closed system is constant, while a prompt opening of the system, e.g., by venting, leads to a mass change, which follows the law of mass conservation [26]:

$$\dot{m}_{\text{gas}} = -\frac{dm}{dt} \quad [\text{g s}^{-1}] \quad (1)$$

where \dot{m}_{gas} is the mass-related gas flow rate out of the container and has to be equal to the change of mass $\frac{dm}{dt}$ inside the container. Usually, the venting is a heterogeneous composition consisting of a solid, vapor, and gaseous phase. In this paper the index "gas" represents all phases and should be considered a substitution. If the venting during TR of a lithium-ion cell is assumed to be an isentropic and represented as ideal gas flow [26], it can be written as

$$\dot{m}_{\text{gas}} = \frac{v_{\text{gas}} p_{\text{gas}} A_{\text{vent}}}{RT_{\text{gas}}} \quad [\text{g s}^{-1}] \quad (2)$$

where v_{gas} is the gas velocity at the vent area A_{vent} , p_{gas} is the gas pressure at the vent area, R is the universal gas constant and T_{gas} is the gas temperature at the vent area. The

assumption of ‘isentropic’ idealizes the venting to be an adiabatic and reversible process, so that the entropy in the beginning and in the end of the process are equal. Equation (2) shows a dependency of vent flow and the fluid dynamics properties such as venting pressure p_{gas} and venting gas temperature T_{gas} . The parameters p_{gas} , T_{gas} and v_{gas} can be determined by making an assumption about the composition of the venting gas and the isotropic flow law with the Equations (20)–(28) from Ref. [27]. Another option is to obtain the parameters by measurement such as pressure sensors, pitot tube, optical methods, temperature sensors, etc. as listed in Table 1.

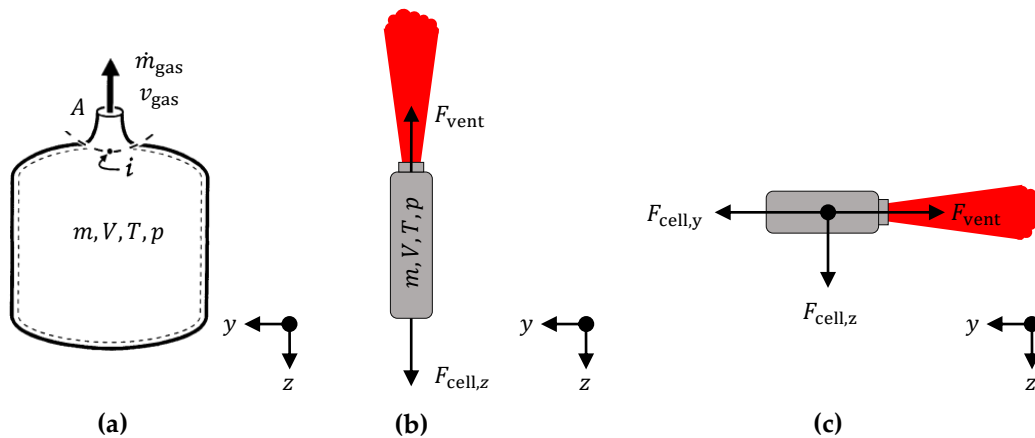


Figure 1. (a) Sketch for venting of a pressure vessel (adapted from [52]). A venting cylindrical lithium-ion cell in (b) vertical and (c) horizontal direction with occurring forces.

In this work we present a mechanical measurement approach based on mass conservation with Equation (1) and Newton’s second and third law as recently published by [47]. The safety valve is the system boundary where an amount of emission leaves the LIB. Assuming the lithium-ion cell as a system and a mass leaves the system, Newton’s third law will apply, implying an equilibrium state between an action and a reaction. In our case, the vent flow creates a force F_{vent} at the vent area (=action) and the lithium-ion cell reacts with an equal opposite force $F_{\text{cell},y}$ (=reaction).

$$F_{\text{vent}} = F_{\text{cell},y} \quad [\text{N}] \quad (3)$$

The venting force occurs due to the motion of gas and ejecta, which is described by Newton’s second law:

$$F_{\text{vent}} = \dot{m}_{\text{gas}} v_{\text{gas}} \quad [\text{N}] \quad (4)$$

Figure 1c shows the venting at the positive cap of the battery and the occurring forces. Due to the venting, the lithium-ion cell loses mass and Equation (1) can be applied. The cell mass m_{cell} at time t can be determined by subtracting venting gas mass m_{gas} from the cell mass at the beginning $m_{\text{cell},0}$ before the venting occurs at time $t = 0$ s.

$$m_{\text{cell}} = m_{\text{cell},0} - m_{\text{gas}} \quad [\text{g}] \quad (5)$$

Equation (4) can be rewritten through Equation (5) as:

$$F_{\text{vent}} = \frac{d(m_{\text{cell},0} - m_{\text{cell}})}{dt} v_{\text{gas}} \quad [\text{N}] \quad (6)$$

If the cell is placed horizontally as illustrated in Figure 1c the vent force F_{vent} can be determined by the recoil force and does not superpose the weight force $F_{\text{cell},z}$ as it would be the case with an arrangement like in Figure 1b. The time-dependent cell mass m_{cell} can be obtained from the weight force of the cell $F_{\text{cell},z} = m_{\text{cell}}g$. Measuring those forces, the gas flow rate and gas velocity can be determined by:

$$\dot{m}_{\text{gas}} = \frac{dF_{\text{cell},z}}{dtg} \quad [\text{g s}^{-1}] \quad (7)$$

$$\begin{aligned} v_{\text{gas}} &= \frac{F_{\text{vent}}}{\dot{m}_{\text{gas}}} \\ &= \frac{F_{\text{cell},y}}{\dot{m}_{\text{gas}}} \\ &= \frac{F_{\text{cell},y}}{dF_{\text{cell},z}} dtg \end{aligned} \quad [\text{m s}^{-1}] \quad (8)$$

where g is the gravitational constant. Equations (7) and (8) show the possibility to gain time-dependent information on the vent flow dynamics without considering the vent pressure and temperature. Only the recoil and weight forces are needed. Therefore, a horizontal cell orientation like in Figure 1c is preferred to determine both forces. If the orientation of venting is vertical as seen in Figure 1b the measured force in z -direction is a superposition of recoil and weight force during TR. Then, Equations (7) and (8) cannot be applied on vertical oriented cells. According to Finegan et al. [53], the venting is highly dynamic and can occur within fractions of seconds which makes a high frequency measurement absolutely necessary.

With this approach, the size and stability of venting area, venting temperature and cell temperature, venting pressure and cell pressure, as well as the composition of the ejecta are irrelevant for deriving the gas velocity and gas flow rate.

3. Experimental

This section describes the realisation of the presented theory into a customized test bench and test procedure. The test bench triggers a TR in an 18650 lithium-ion cell by overheating and also measures the occurring forces and temperatures.

3.1. Test Bench

Figure 2 is a sketch of the developed test bench and prepared test cells to characterize the dynamic flow of cell venting during TR. To measure the recoil and weight force of the cell during TR, the cell is placed in the cell holder ① made of aluminum with a wall thickness of 3 mm. The cell holder has the function of transmitting the applied heat into the cell, holding the cell at a defined position, achieving a directed venting, and absorbing the recoil force of cell venting to the three-axial force sensor K3D60a ② made by ME Meßsysteme GmbH. The importance of the mechanical support is also mentioned by [47]. The integrated force sensor exists of three strain gauges with a measuring range of ± 20 N on each axis. Between the force sensor and the cell holder are a mechanical transmission plate ③, four small racks and an isolation plate ④. The transmission plate is made of aluminum and transmits the forces occurring at the cell holder in x , y and z -direction through its plate and four small racks. This part is separated from the force sensor with an thermal isolation plate, which protects the force sensor against high temperatures, because it would exceed the operating temperature range of the force sensor, as the cell temperature values can reach 500 °C and more [17,33,54,55] and would exceed the operating temperature range of the force sensor given from -10 to 85 °C.

Usually, calorimeters [1,54,56], heat foils and plates [28,56–58] are used to overheat and trigger the TR of a battery. Garcia et al. [49] used hot flow in a continuous flow vessel, which is a comparable trigger method to a heat gun. The heat gun ⑤, which can operate up to 600 °C is used to heat the cell holder by convection heat transfer and the cell temperature increases through conduction. The flat nozzle of the heat gun is pointed on the vertical center of the cell cross section and placed 22.5 mm in x -direction in front of the cell holder. To protect the force sensor against hot air from the heat gun and hot ejection from the cell venting, a 1 mm thick steel safety plate ⑥ with four holes is installed between the thermal isolation plate and the mechanical transmission plate. The holes are designed as small as

possible but decoupled from the mechanical transmission path between cell holder and force sensor.

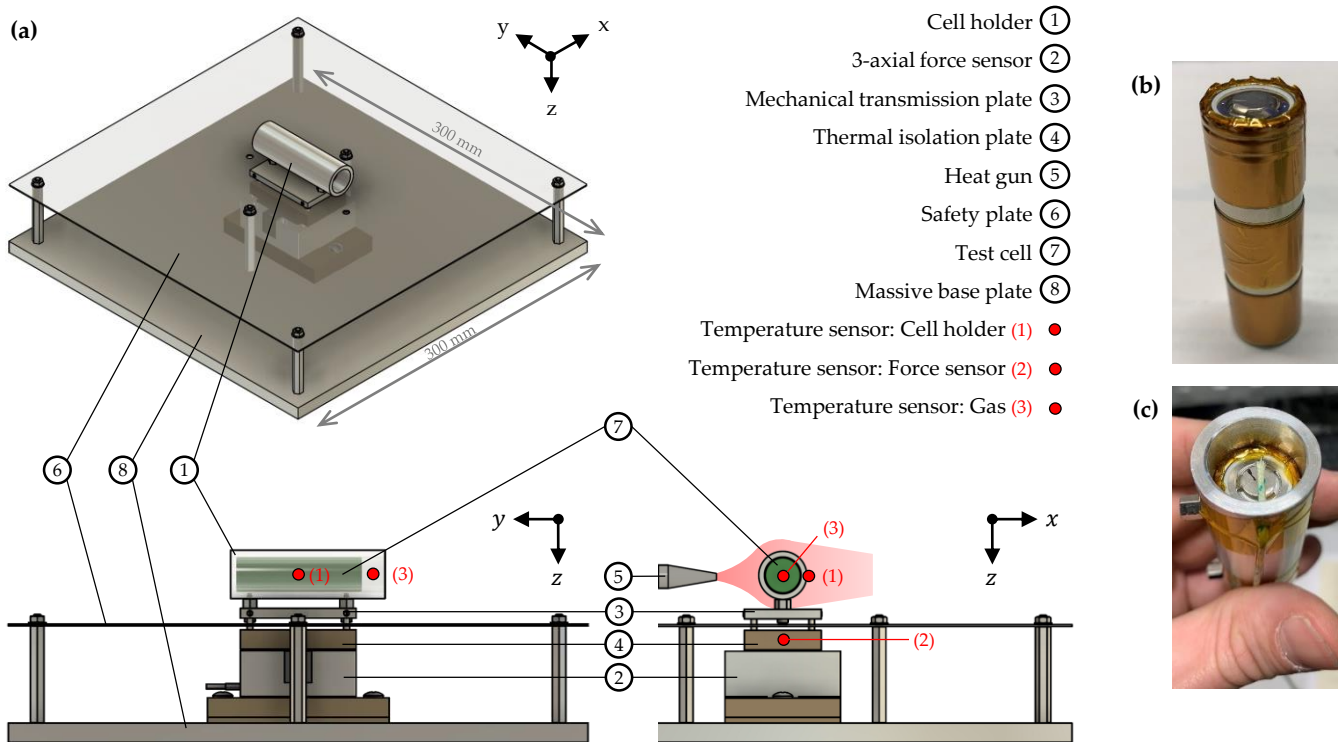


Figure 2. (a) Test bench setup for characterizing the dynamic of vent flow during TR of a cylindrical lithium-ion cell. (b) Example of a prepared test cell. (c) Cell placed in cell holder with temperature sensor.

Three K-type thermocouples measure the temperature near the cell surface (1), the force sensor (2) and the venting gas temperature (3). They are respectively placed at center height of the cell holder on the opposite side to the heat gun in x-direction, inside the thermal isolation plate and 5 mm in front of the positive cell cap. The temperature sensors are logged by a differential multiplexer with a recording temperature range up to 1000 °C with 100 Hz. Furthermore, a video camera captures the thermal abuse process.

With the presented test bench the cell mass at $t = 0$ s, the actual cell mass during the test and the venting force F_{vent} are derived from the force in z-direction $F_{\text{cell},z,0}$ and $F_{\text{cell},z}$ respectively the recoil force in y-direction $F_{\text{cell},y}$. By measuring those parameters, the mass flow rate and gas velocity during venting can be determined with Equations (7) and (8).

To achieve a high accuracy, the forces are logged by the Keysight 34470A digital multimeters (DMM) with at least 10 Hz and $7\frac{1}{2}$ digits of resolution. Additionally, the PicoScope 5442D oscilloscope (Osci) is used to record the forces with 14 bit, but with a sampling rate of 10 kHz achieving a high time resolution as well. This test setup allows observation of venting and TR events in the time range from 100 μ s to minutes. The measurement chain from force sensor via measurement amplifier to the data loggers was calibrated. So that the linearity deviation of the force sensor, given with 0.2%, is improved to 0.12% more specifically ± 2.45 g over the full range of each axis.

3.2. Test Cells and Test Procedure

Two different cylindrical 18650 cells are used to measure the ejection parameters. The cell specifications are listed in Table 2. The high energy lithium-ion cell INR18650LGMJ1 manufactured by LG Chem Ltd. (Seoul, Republic of Korea) has a silicon-graphite anode and a NMC₈₁₁ cathode [59] with a nominal capacity of 3.5 Ah. The second cell type is the high-power cell US18650VTC5A by Sony made of a silicon-graphite anode and

a $\text{LiNi}_{0.80}\text{Co}_{0.15}\text{Al}_{0.05}\text{O}_2$ (NCA) cathode [60] with a nominal capacity of 2.5 Ah. In the following, they are named LGMJ1 and SonyVTC5A, respectively.

Five SonyVTC5A cells and five LGMJ1 cells were tested at 100% state of charge (SoC). The precision balance TE313S by Sartorius with 0.001 g accuracy was used to weigh the cell before the test and showed an average mass of 47.937 g for SonyVTC5A and 46.880 g for LGMJ1 (see Table 2). Afterwards, the cell were prepared by dismantling the plastic envelope and wrapping up in Kapton tape to achieve a good stiff mechanical and thermal contact in the cell holder, as seen in Figure 2c. Furthermore, the Kapton tape functions as an electrical isolation to avoid external short circuits. Approximately 1.398 g and 1.148 g Kapton tape were attached to SonyVTC5A and LGMJ1, respectively. SonyVTC5A cells needed more Kapton tape due to the lower cell diameter.

Table 2. Specifications of investigated 18650 format cells. The mass is a measured average value of the tested cells. The dismantled plastic envelope weighs approximately 0.456 g for SonyVTC5A and 0.461 g for LGMJ1.

		US18650VTC5A (Sony)	INR18650 MJ1 (LG)
Dimensions	mm	∅18.35;65.0	∅18.5;65.1
Cathode chemistry		NCA [60]	NMC ₈₁₁ [59]
Anode chemistry		Graphite + Silicon [60]	Graphite + Silicon [59]
Nominal voltage	V	3.6	3.64
Nominal capacity	Ah	2.5	3.5
Vent cap holes		3	4
Number of cells		5	5
Mass	g	47.937	46.880
Mass without isolation	g	47.483	46.417
Mass without isolation with Kapton tape	g	48.881	47.565

The experiments with the customized test bench were carried out in a safety bunker. The prepared cell was placed into the cell holder with the negative pole facing into the cell holder. So that the venting and TR is forced to happen at the safety valve at the positive cap. Then, the temperature sensors are attached with Kapton tape measuring the gas temperature and the temperature at the cell holder. The heat gun is controlled by the surface temperature of the cell holder, as shown in Figure 3. The heat gun heated the cell holder up to $T_{\text{cell holder}} = 100^\circ\text{C}$ and paused afterwards for 20 s. Then, a heat-wait mode was applied, where the temperatures [120 °C; 140 °C; 160 °C; 180 °C; 200 °C] were achieved one after another followed by a 20 s pause in between. The heating was stopped immediately when safety valve opened.

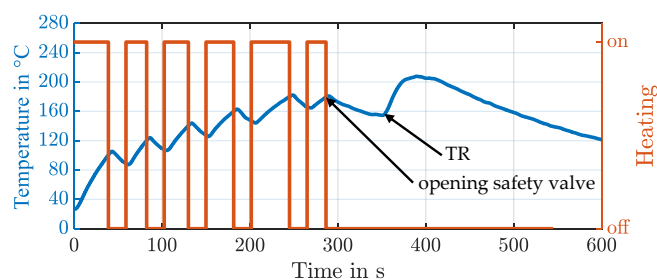


Figure 3. Visualisation of the applied heating method to trigger TR of lithium-ion cells by overheating. The heating is controlled by the temperature of the cell holder. At approximately 160–180 °C safety valve opened and the heat gun was switched off immediately.

4. Results

4.1. Overheating and Initiation of Thermal Runaway

For each cell types, five TR experiments by overheating were conducted. Figure 4 shows snapshots from the recorded video of SonyVTC5A sample #5. According to Zhou et al. [41] and Wang et al. [34] the presented thermal abuse can be categorized into five stages: heating, opening safety vent, transition, TR and abatement. In our experiments no visual changes were observed during heating stage. When the safety valve opened, a leak with a sudden venting occurred. This incident is followed by the transition stage where the venting turns into white smoke. Thereafter, the cell goes into TR and can show phenomena of violent venting, jets, hot ejecta, burning, flames and might end in an explosion or a stable combustion. In our experiments the latter occurred. The end of the abuse process is given by the abatement stage.

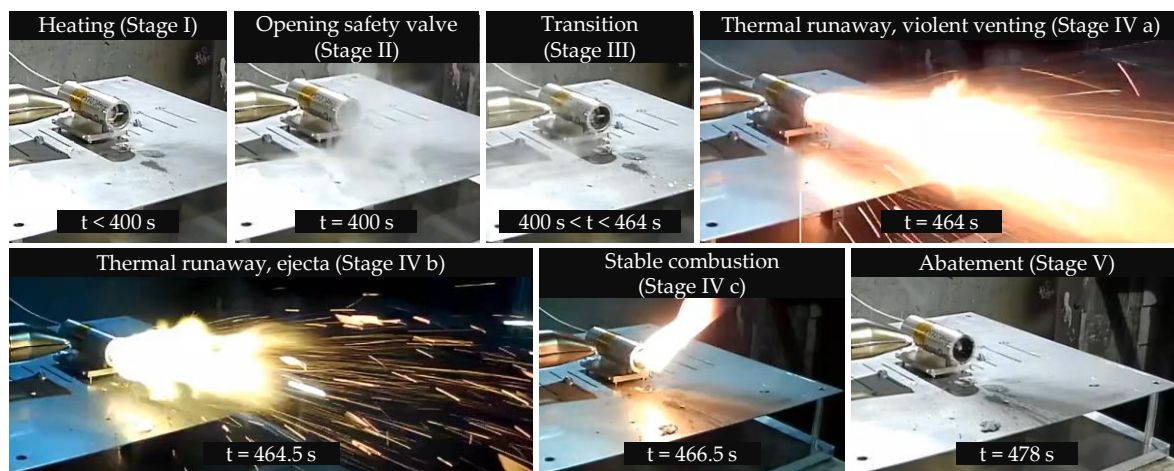


Figure 4. Typical phenomena of TR test using the example of SonyVTC5A sample #5. The division in stages is adapted from [41].

Figure 5a–h shows an overview of the temperature profiles and force responses of all tests. To compare the tests of each cell type the data are synchronized by the opening of the safety valve, which happens to be at 400 s and 300 s for SonyVTC5A cells and LGMJ1 cells, respectively. With the presented heating mode in Figure 3, the cell holder with the cell sample were heated up to 180 °C within approximately 4–4.5 min. Three LGMJ1 cells needed to be reheated after the cell cooled down during transition stage and an absent TR. Therefore, we conducted heat-wait-see tests in an accelerated rate calorimeter, which showed that the TR in LGMJ1 cells occurs at a temperature of approximately 192.8 °C. However, the opening of the safety valve in our test bench happened at a cell holder temperature lower than 190 °C. Perhaps, the ongoing reactions inside the cell during the transition stage did not always accelerate the inner cell temperature due to inhomogeneous temperature distribution or an effective, non-clogged and safe venting by the opening of safety valve. Therefore, the trigger temperature of TR, which starts uncontrollable reactions such as cathode decomposition [61], was not crossed for the reheated LGMJ1 cells in the first place.

In general, after the safety valve opens and smoke passes out the cell, the cell holder temperature decreases slowly, whereas the gas temperature remains stable until the second incident — the TR event — occurs (see Figure 5a–d). It can be identified by a skyrocketing behavior of the gas temperature due to violent venting of flammable gas and ejecta while the cell holder temperature increase is damped and stays below 300 °C. Finally, the high dynamic thermal behavior abates. Comparing temperature curves of all samples, small variations like short time delays or different peak values exist. Even though the curves do not perfectly overlap, the tendencies are the same. In Section 4.3 the characteristic temperatures will be discussed in detail.

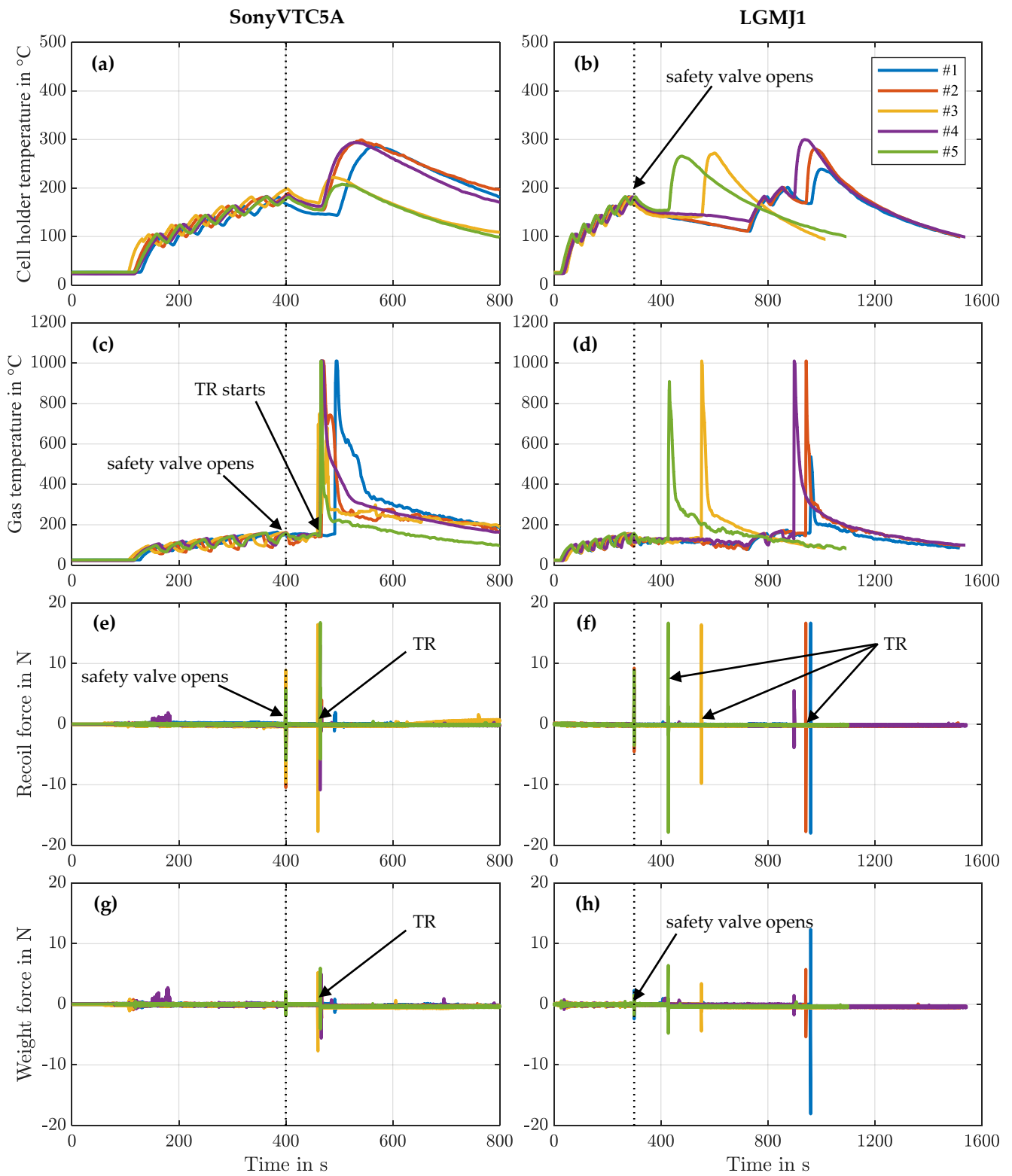


Figure 5. Measured temperatures (a–d) and forces (e–h) during thermal abuse by overheating for SonyVTC5A cells (left column) and LGMJ1 cells (right column). Data are synchronized at the opening of the safety valve (dotted vertical line). (a,b) temperature of the cell holder. (c,d) gas temperature. (e,f) recoil force in y-direction. (g,h) weight force in z-direction. The plotted force data are from oscilloscope.

In addition, the two incidents can also be detected by the force sensors. Figure 5e–h shows for all test samples two force peaks appearing immediately along with the opening of the safety valve and TR. Therefore, the force response is a good way to identify the incidents and get an accurate determination of the transition time. It took 69.46 ± 12.67 s for the SonyVTC5A cells to go from opening of the safety valve into TR, whereas the non-reheated LGMJ1 cells needed 189.54 ± 87.56 s. The results are in good agreement with the reported value range from 120–175 s of cylindrical NMC cells [9,33,50,51] and with the finding by Ohneseit et al. [62] that TR occurs earlier at NCA cells than NMC cells. The transition time is a valuable parameter for designing early warning systems and safety assessment of battery packs.

To clarify, Figure 5e–h shows only the force data logged by the oscilloscope, because there was no reliable detection of the first venting by the opening of the safety valve with DMM. Huang et al. [28] reported that the venting process at the opening of safety valve takes 0.064 s for a 21700 format battery with NCA as cathode chemistry. Additionally, in our work the DMM recorded every 0.1 s which means the force response at the first venting last less than 0.1 s.

4.2. Observed Mass Loss

During the thermal abuse process, the cell vents and loses mass. The cell mass change corresponds to the gas flow rate of the venting and can be determined by Equation (7) with the force response in z-direction. For the first vent no lasting changes of the cell weight were detected, either with Osci nor with DMM. Taking the accuracy of the test bench into account, only mass changes larger than ± 2.45 g can be noticed accurately. Huang et al. [28] reported that the first venting takes 0.064 s for a 21700 format battery with a mass flow rate of 8.375 gs^{-1} . Consequently, 0.536 g mass was ejected in their study and is around five times lower than the accuracy of our force sensor.

Therefore, we take a closer look at the mass loss during TR stage. Figure 6 shows the force responses of one test sample of each cell types in y- and z-direction for TR stage in detail. The original force signals of the Osci with 10 kHz are highly noisy. Improvements can already be made with a lowpass filter by 100 Hz. Nevertheless, to determine the mass loss m_{loss} , the force in z-direction before $F_{z,\text{before TR}}$ and after $F_{z,\text{after TR}}$ the TR event were used.

$$m_{\text{loss}} = \frac{(F_{z,\text{before TR}} - F_{z,\text{after TR}})}{g} = \frac{\Delta F_z}{g} \quad [\text{g}] \quad (9)$$

In Figure 6c,d the force changes $\Delta F_{z,\text{Osci}}$ and $\Delta F_{z,\text{DMM}}$ for both datalogger are marked. The boxplots (e) and (f) underneath show averaged mass losses with the Osci for SonyVTC5A and LGMJ1 of 57.50% and 63.45%, respectively. The values determined by the DMM are similar with 56.61% and 62.89% for SonyVTC5A and LGMJ1, respectively. Although the DMM data have a higher resolution than the Osci data, nearly the same results were achieved. The application of DMM has also disadvantages such as limited measurement frequency, pricier, limited data readings and the need of data synchronisation. Taking the benefits and limitations of DMM and comparison of the results on the mass loss during TR into account, the oscilloscope is the better datalogger and was validated by the DMM.

Besides the mass loss during TR we determined the total mass loss. Therefore, each cell was weighted before and after the thermal abuse test using a precise mass balance with an accuracy of ± 0.001 g. The total mass loss lays between 55.88% and 81.64% for SonyVTC5A and 50.49% up to 74.28% for LGMJ1. It is covering the mass loss of all stages during the thermal abuse process. The National Renewable Energy Laboratory (NREL) and National Aeronautics and Space Administration (NASA) published an open-source Battery Failure Databank (BFD) [63] containing data from a wide range of thermal abuse tests with the Fractional Thermal Runaway Calorimeter (FTRC) developed by Walker et al. [1]. The BFD reports total mass losses between 63.88% and 85.70% for Sony 18650-VTC6 cells and

57.02% up to 83.83% for LG 18650-MJ1 cells triggered by overheating and showing a good agreement with our presented total mass losses.

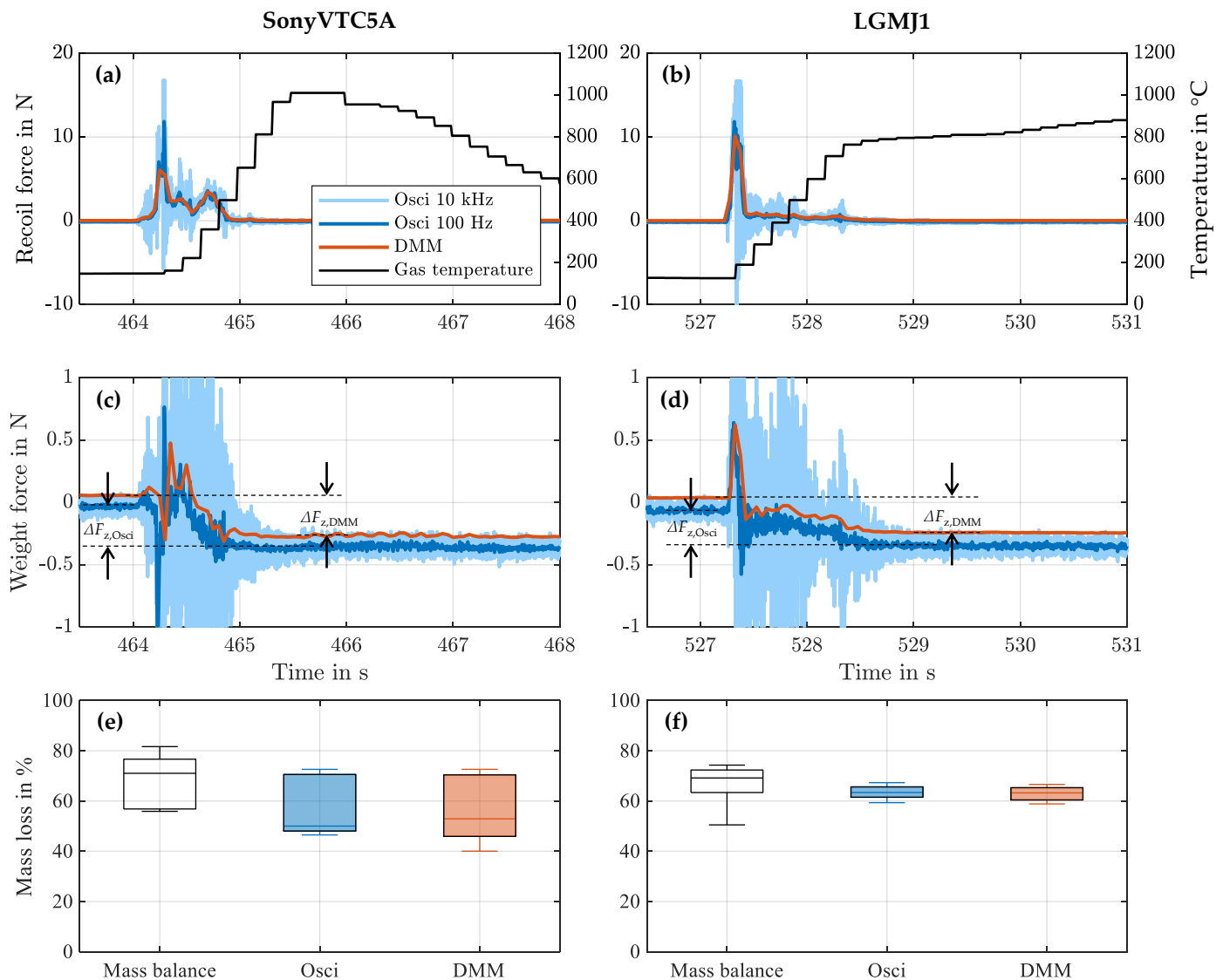


Figure 6. Force response in y- and z-direction during the stage of TR exemplary with sample #5 and the measured percentage mass loss by Osci and DMM during the stage of TR for (left column) SonyVTC5A and (right column) LGMJ1. (a,b) show the recoil force in y-direction. (c,d) show the weight force in z-direction. (e,f) display the distribution of mass loss. The mass loss measured by the precise mass balance is the total mass loss of the cell covering the losses from opening safety valve to TR to abatement.

4.3. Fluid Mechanical Parameters of Venting

In this section, the measured and determined fluid mechanical parameters of venting such as gas temperature, gas flow rate, and gas velocity are described. Figure 7 presents the temperature distribution of the first venting, TR and the maximum values. The maximum temperatures occurred always during TR stage, and the gas temperature exceeded the upper measuring limit of the data logger of 1000 °C. Obviously higher temperature were present. Whereas, the temperature of cell holder achieved approximately 262 °C and 272 °C for SonyVTC5A and LGMJ1, respectively. During the heating, the cell holder temperature does not entirely correspond with the cell temperature and is affected by the thermal contact between the cell holder and cell sample. With the heating pauses the gap becomes smaller

and the cell gets the chance to thermally homogenise by heat conduction. Nevertheless, when the safety valve opens, the cell holder temperature was in average 182.01°C for the high-power battery and 171.57°C for the high-energy battery. Those values agree with reported onset temperatures for the first venting of cylindrical NMC cells [17,33,49,55]. In the transition stage the cell holder temperature decreased to 160°C for both cell types, while the gas temperature of the high-power cell remained almost constant at $150.16 \pm 5.40^\circ\text{C}$, while a slight increase up to $136.73 \pm 18.50^\circ\text{C}$ for the high-energy cell was detected.

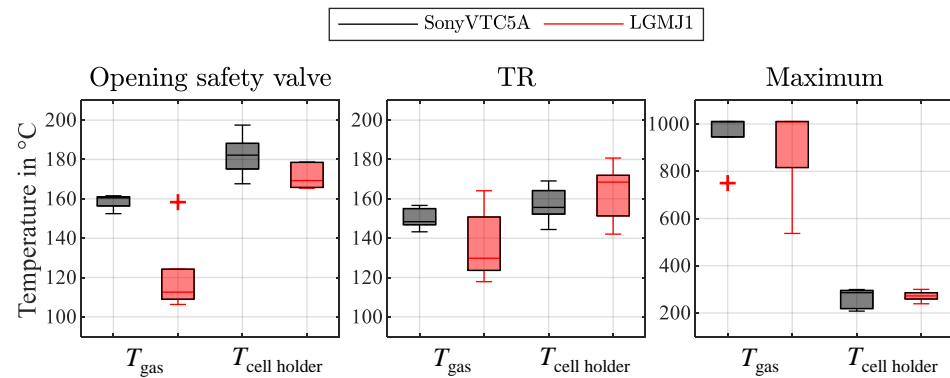


Figure 7. Temperature distribution of gas and cell holder regarding the opening of safety valve, TR and maximum value for both cell types. The + are showing an outlier that is more than 1.5 times of the interquartile range away from the top or bottom of the box.

Characterizing the venting incidents regarding their intensity, the maximum forces can take into consideration. Figure 8 illustrates the recoil force distribution. The distributions are similar for both cell types at the opening of safety valve. The average values are 6.41 N and 7.34 N. Whereas, the recoil force during TR were detected along the full force range for high-power battery or exceeding the upper force limit.

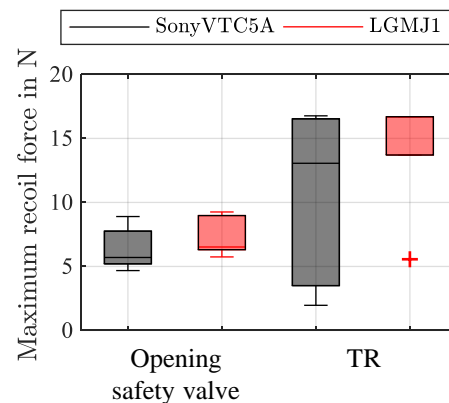


Figure 8. Distribution of maximum recoil force occurring at opening safety valve and TR for both cell types. The + are showing an outlier that is more than 1.5 times of the interquartile range away from the top or bottom of the box.

Figure 9a–d are giving a closer look at the recoil force response during TR event. As mentioned before, the force curves logged by Osci are too noisy to be used in time-dependent calculations such as Equations (7) and (8). Therefore, filtering gets important and a lowpass filter with 100 Hz was used. The TR end is defined by the time when the recoil force reaches its original value from before the TR $F_{y,\text{beforeTR}}$ and considering the error of the measurement chain $e_{\text{meas}} = \pm 2.45 \text{ g}$. The mean values and standard deviation of the TR duration are listed in Table 3. The rebound effect in the weight force signal (see Figure 6c,d) could be a crosstalk of the recoil force which is according to the datasheet and

manufacturer 1–2%. To gain the gas flow rate as proposed in Equation (7), the method like Huang et al. [28] used to determine the mass flow rate at the first venting is used. Therefore, the gas flow rate is linearized by dividing the change in the weight force $\Delta F_{z,Osci}$ by the TR duration $\Delta t_{TR} = t_{TR,end} - t_{TR,start}$. Next, the gas velocity for both cell types can be determined with the linearized gas flow rate and Equation (8). The time-resolved gas velocity for one sample of each cell types at TR stage are shown in Figure 9e. The shape of the velocity curve differs for the cell types, but the first peak which is a maximum and occurs in the first-third. The value of the maximum velocity depends on the TR duration Δt_{TR} which affects the value of the linearized gas flow rate. Therefore, it is important to consider the definition of the force threshold which marks the end of change in the recoil force during the TR event. A narrow threshold would increase the TR duration and result in a lower maximum gas velocity. The qualitative progress of the gas velocity is affected by the curve shape of the recoil force. The gas velocity of LGMJ1 cells follows a single peak asymmetrical pattern and for the SonyVTC5A a bumpy pattern with two or three bumps. Table 3 summarizes the derived fluid mechanical parameters of venting at the TR stage for both cell types and taking all samples into account.

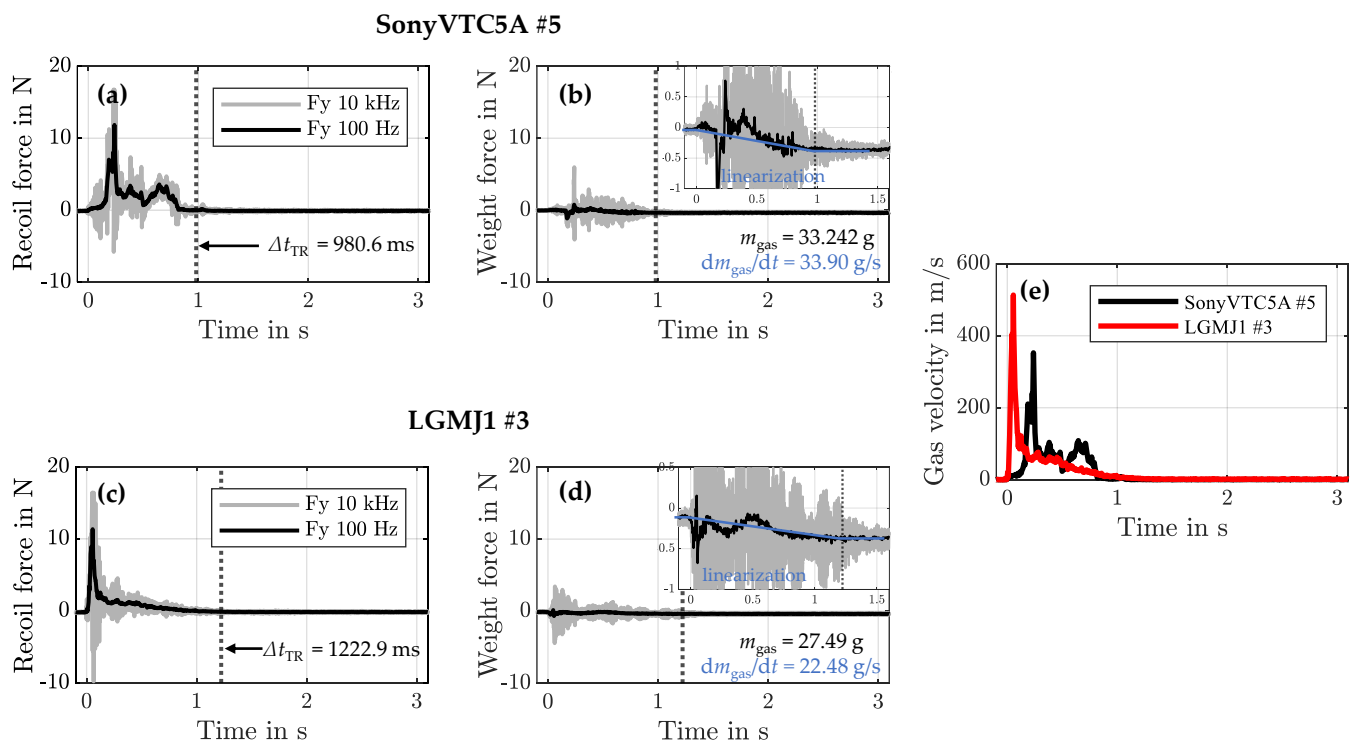


Figure 9. Recoil force (a,c) and weight force (b,d) exemplary of SonyVTC5A sample #5 and LGMJ1 sample #3 during TR stage with original measuring frequency of 10 kHz and as lowpass filtered signal with 100 Hz. Duration of TR Δt_{TR} marks the time when the recoil force reaches the threshold $F_{thold} = (F_{y,beforeTR} + e_{meas})$. The gas flow rate is linearized as presented in the snapshot. (e) determined gas velocity during TR event with Equation (8) of SonyVTC5A sample #5 and LGMJ1 sample #3. The data are synchronized by setting the start of TR event to $t = 0$ s.

Table 3. Results for the venting properties with TR duration Δt_{TR} , mass loss m_{loss} , gas flow rate \dot{m}_{gas} , maximum gas velocity $v_{gas,max}$ and the velocity curve shape for the TR stage.

	SonyVTC5A	LGMJ1
Mass loss at TR m_{loss}	27.30 ± 5.999 g	29.45 ± 1.390 g
TR duration Δt_{TR}	1718 ± 1002 ms	1131 ± 290.9 ms
Gas flow rate \dot{m}_{gas}	22.15 ± 14.70 g/s ⁻¹	27.92 ± 9.500 g/s ⁻¹

Table 3. Cont.

	SonyVTC5A	LGMJ1
Maximum gas velocity $v_{\text{gas,max}}$	$260.9 \pm 103.5 \text{ ms}^{-1}$	$398.5 \pm 207.1 \text{ ms}^{-1}$
Velocity curve shape	bumpy pattern with two to three bumps	single peak asymmetrical pattern

5. Discussion

With the developed test bench two sets of parameters of the venting properties were obtained for 18650 format cell types, see Table 3. To verify and validate the main findings, the gas flow rate and gas venting velocity will be compared to experimental and simulative research results. The method we applied to characterize the venting was recently published by Li et al. [47] who determined a time-dependent gas velocity for a NMC prismatic LIB which follows a single peak symmetrical pattern with a maximum velocity of 210.86 ms^{-1} . The TR stage lasted approximately 14 s and a maximum gas flow rate of 41 gs^{-1} was obtained. Other research on large-format prismatic LIBs reported a similar velocity progression over time for the TR stage, but that the maximum gas venting velocity occurs at the opening of the safety valve [34,41,43,45]. In our study we detected a single peak asymmetrical velocity pattern for the high-energy cylindrical LIB and a TR duration lower than 1.5 s. Besides the cell format, the different venting behavior during TR can also be affected by other factors, such as the shape and type of the safety valve, as reported by [43]. A symmetrical velocity pattern occurs at oval and round safety valves which are mostly used in prismatic LIBs, whereas an asymmetrical velocity progress with the highest velocity peak developed with a cavity safety valve and is common in cylindrical LIBs [43]. Those findings make a comparison difficult.

Because of that, only comparisons with an equal cell format will be discussed in the following. Garcia et al. [49–51] used optical methods and monitored maximum jet velocities between $30\text{--}50 \text{ ms}^{-1}$, which are almost ten times lower than ours (see Table 3). Optical methods measure the velocity beyond the vent area, whereas the momentum and mass conservation method obtains information of the venting at the vent area. Additionally, optical methods can investigate the venting as long as no wall interactions appears, which is mostly limited to a few milliseconds [50].

Venting and TRP models, which consider venting, use the venting properties gas flow rate and gas velocity as interim parameters to couple models on cell domain level with CFD models. In the studies from [31–33,35,36] the simulated maximum vent flow velocities are almost always in the same order of magnitude to our measured velocities and range from 85 ms^{-1} [31] to approximately $162\text{--}178.3 \text{ ms}^{-1}$ [32,33,35], or even up to 340 ms^{-1} in some cases [36]. However, there are differences in the TR duration and gas flow rate. The TR lasted more than five seconds except in the study from Mishra et al. [36], where it took 2.27 s which is comparable to our measured TR duration with $1.718 \pm 1.002 \text{ s}$ for high-power and $1.131 \pm 0.2909 \text{ s}$ for high-energy LIBs. However, the simulated gas flow rates are given with 2.5 gs^{-1} [31] to 3.5 gs^{-1} [35] and one order of magnitude lower than our measured gas flow distribution with $22.15 \pm 14.70 \text{ gs}^{-1}$ for SonyVTC5A and $27.92 \pm 9.500 \text{ gs}^{-1}$ for LGMJ1 cells.

With the developed test bench we are able to narrow the lack of research on the venting characteristics of 18650 LIBs and achieved reliable and reproducible set of parameters for the venting properties during TR triggered by overheating. Any kind of 18650 format LIB can be tested regardless of the cell chemistry or capacity. The applied method uses the principles of momentum and mass conservation, and with modifications on the cell holder and range of force sensors different cell formats can be tested. If a pouch cell or a cell without a safety valve should be tested, a cell holder would act like a hard case causing a predefined direct venting and might represent an effective way comparing the test method for different cell formats and types. Additionally, the vent area can have any size and form, and does not have to be constant during the TR process as it is assumed in venting models

or in the pressure-based methods. Overheating was the chosen trigger method in our work, but other thermal triggers, e.g., heater or laser, and electrical triggers can be applied, as long as the force sensor is kept in his operating temperature range. The customized test bench is extendable with further measurement equipment, e.g., voltage monitoring, optical devices, gas analyzer, as long as the vent flow is not distracted.

However, there is potential to optimize the test setup. On the one hand, the recoil force of the LGMJ1 cells exceeded the force measurement range in some cases. On the other hand, the resolution of the force sensor with ± 2.45 g is limiting the measurement in z-direction. Regarding the minimum mass loss during thermal abuse a resolution of at least ± 0.5 g and two different ranges for the force sensor in y- and z-direction should be considered when choosing the sensor. As mentioned before, electrical and thermal trigger method can be implemented, while mechanical trigger, e.g., nail penetration, would affect the force measurement with an overlapped force response and would make it difficult to extract the venting parameters.

Considering the benefits and limitations of the presented work, the method and test bench have a great potential contributing more insights in the venting behavior, characterizing the venting during the abuse process and supporting the battery safety hazard assessment.

6. Conclusions

In this work we characterized the venting during thermal abuse triggered by overheating of two 18650 format cell types. We developed and built a test bench based on the principles of the momentum and mass conservation method. The test bench allowed us to run reliable and reproducible tests and provides valuable findings. Firstly, we found that the force sensor can be used as an identification option for incidents such as ventings. Secondly, our tests show that the curve shape of the gas velocity varies for the cell types. The high-energy cell follows a single peak asymmetrical pattern, while the high-power cell vents with a bumpy pattern with two or three bumps. Thirdly, we measured the transition time between the safety venting and TR and determined that the time from the first venting to TR for the high-energy LIB is at least twice as long as for the high-power LIB. Those results are valuable for designing early warning systems. Finally, we presented sets of parameters for the venting properties of a high-energy and a high-power 18650 format LIB, that can be used for battery safety hazard assessments, simulations and pack design studies.

With some modifications to the test bench, the characterization method can be applied to other cell formats, cell chemistries and capacities. Even scaling up to test a battery module seems possible. In addition, other thermal and electrical trigger methods of TR can be realized.

Author Contributions: Conceptualization, E.I.G.; methodology, E.I.G.; software, E.I.G.; validation, E.I.G.; formal analysis, E.I.G.; investigation, E.I.G. and M.S.; resources, A.J.; data curation, E.I.G.; writing—original draft preparation, E.I.G.; writing—review and editing, E.I.G., M.S., Y.F. and A.J.; visualization, E.I.G.; supervision, A.J.; project administration, E.I.G. and A.J.; funding acquisition, A.J. All authors have read and agreed to the published version of the manuscript.

Funding: This research was supported financially by the German Federal Ministry of Education and Research (BMBF) [03XP0322B NUBase] and Federal Ministry for Economic Affairs and Energy (BMWi) [03ET6153C iMoBatt].

Data Availability Statement: The data presented in this study are available on request from the corresponding author. The data are not publicly available due to privacy policy.

Acknowledgments: The authors gratefully thank Andreas Noel for supporting the conceptualization and the measurement setup. Further thanks go to Jens Dietrich and Korbinian Schmidt for their practical support and Oliver Höcklin for assisting the preparatory work.

Conflicts of Interest: The authors declare no conflict of interest. The funders had no role in the design of the study; in the collection, analyses, or interpretation of data; in the writing of the manuscript; or in the decision to publish the results.

Abbreviations

The following abbreviations are used in this manuscript:

Acronyms

BFD	Battery Failure Databank
CFD	computational fluid dynamics
DMM	digital multimeter
FTRC	Fractional Thermal Runaway Calorimeter
LCO	lithium-cobalt-oxide
LFP	lithium-iron-phosphate
LIB	lithium-ion battery
NASA	National Aeronautics and Space Administration
NCA	nickel-cobalt-aluminum-oxide
NMC	nickel-cobalt-manganate
NREL	National Renewable Energy Laboratory
Osci	oscilloscope
SEI	solid-electrolyte interphase
SoC	state of charge
TR	thermal runaway
TRP	thermal runaway propagation

Symbols

A_{vent}	vent area, m^2
e_{meas}	error of measurement chain, N
$\Delta F_{z,Osci}$	force change with oscilloscope, N
$\Delta F_{z,DMM}$	force change with digital multimeter, N
Δt_{TR}	thermal runaway duration, s
$F_{cell,y}$	recoil force, force in y-direction, N
$F_{cell,z}$	weight force, force in z-direction, N
F_{thold}	threshold force, N
F_{vent}	vent force, N
$F_{y,beforeTR}$	vent force before TR event, N
$F_{z,before TR}$	weight force before TR, N
$F_{z,after TR}$	weight force after TR, N
g	gravitational constant, 9.81 Nkg^{-1}
m	mass, g
m_{cell}	cell mass, g
$m_{cell,0}$	cell mass at time $t = 0$ s, g
m_{gas}	venting gas mass, g
m_{loss}	mass loss, g
\dot{m}_{gas}	gas flow rate, gs^{-1}
p	pressure, Nm^{-2}
p_{gas}	gas pressure, Nm^{-2}
R	universal gas constant, $8.314 \text{ Jmol}^{-1}\text{K}^{-1}$
t	time, s
$T_{cell holder}$	cell holder temperature, $^{\circ}\text{C}$
T_{gas}	gas temperature, $^{\circ}\text{C}$
$t_{TR,end}$	thermal runaway event ends, s
$t_{TR,start}$	thermal runaway event starts, s
V	volume, m^3

v_{gas}	gas velocity, ms^{-1}
$v_{\text{gas,max}}$	maximum gas velocity, ms^{-1}

References

- Walker, W.Q.; Darst, J.J.; Finegan, D.P.; Bayles, G.A.; Johnson, K.L.; Darcy, E.C.; Rickman, S.L. Decoupling of heat generated from ejected and non-ejected contents of 18650-format lithium-ion cells using statistical methods. *J. Power Sources* **2019**, *415*, 207–218. [\[CrossRef\]](#)
- Doughty, D.H.; Roth, E.P. A General Discussion of Li Ion Battery Safety. *Electrochem. Soc. Interface* **2012**, *21*, 37. [\[CrossRef\]](#)
- Pegel, H.; Schaeffler, S.; Jossen, A.; Sauer, D.U. Extensive Experimental Thermal Runaway and Thermal Propagation Characterization of Large-Format Tabless Cylindrical Lithium-Ion Cells with Aluminum Housing and Laser Welded Endcaps. *J. Electrochem. Soc.* **2023**, *170*, 120512. [\[CrossRef\]](#)
- Lammer, M.; Königseder, A.; Hacker, V. Holistic methodology for characterisation of the thermally induced failure of commercially available 18650 lithium ion cells. *RSC Adv.* **2017**, *7*, 24425–24429. [\[CrossRef\]](#)
- Finegan, D.P.; Darst, J.; Walker, W.; Li, Q.; Yang, C.; Jervis, R.; Heenan, T.M.; Hack, J.; Thomas, J.C.; Rack, A.; et al. Modelling and experiments to identify high-risk failure scenarios for testing the safety of lithium-ion cells. *J. Power Sources* **2019**, *417*, 29–41. [\[CrossRef\]](#)
- Hou, J.; Feng, X.; Wang, L.; Liu, X.; Ohma, A.; Lu, L.; Ren, D.; Huang, W.; Li, Y.; Yi, M.; et al. Unlocking the self-supported thermal runaway of high-energy lithium-ion batteries. *Energy Storage Mater.* **2021**, *39*, 395–402. [\[CrossRef\]](#)
- Liu, X.; Stolarov, S.I.; Denlinger, M.; Masias, A.; Snyder, K. Comprehensive calorimetry of the thermally-induced failure of a lithium ion battery. *J. Power Sources* **2015**, *280*, 516–525. [\[CrossRef\]](#)
- Wang, Z.; Ning, X.; Zhu, K.; Hu, J.; Yang, H.; Wang, J. Evaluating the thermal failure risk of large-format lithium-ion batteries using a cone calorimeter. *J. Fire Sci.* **2019**, *37*, 81–95. [\[CrossRef\]](#)
- Zhong, G.; Mao, B.; Wang, C.; Jiang, L.; Xu, K.; Sun, J.; Wang, Q. Thermal runaway and fire behavior investigation of lithium ion batteries using modified cone calorimeter. *J. Therm. Anal. Calorim.* **2019**, *135*, 2879–2889. [\[CrossRef\]](#)
- Wang, S.; Rafiz, K.; Liu, J.; Jin, Y.; Lin, J.Y.S. Effects of lithium dendrites on thermal runaway and gassing of LiFePO₄ batteries. *Sustain. Energy Fuels* **2020**, *4*, 2342–2351. [\[CrossRef\]](#)
- Ren, D.; Hsu, H.; Li, R.; Feng, X.; Guo, D.; Han, X.; Lu, L.; He, X.; Gao, S.; Hou, J.; et al. A comparative investigation of aging effects on thermal runaway behavior of lithium-ion batteries. *eTransportation* **2019**, *2*, 100034. [\[CrossRef\]](#)
- Finegan, D.P.; Scheel, M.; Robinson, J.B.; Tjaden, B.; Hunt, I.; Mason, T.J.; Millichamp, J.; Di Michiel, M.; Offer, G.J.; Hinds, G.; et al. In-operando high-speed tomography of lithium-ion batteries during thermal runaway. *Nat. Commun.* **2015**, *6*, 6924. [\[CrossRef\]](#) [\[PubMed\]](#)
- Finegan, D.P.; Darcy, E.; Keyser, M.; Tjaden, B.; Heenan, T.M.M.; Jervis, R.; Bailey, J.J.; Malik, R.; Vo, N.T.; Magdysyuk, O.V.; et al. Characterising thermal runaway within lithium-ion cells by inducing and monitoring internal short circuits. *Energy Environ. Sci.* **2017**, *10*, 1377–1388. [\[CrossRef\]](#)
- Finegan, D.P.; Darcy, E.; Keyser, M.; Tjaden, B.; Heenan, T.M.M.; Jervis, R.; Bailey, J.J.; Vo, N.T.; Magdysyuk, O.V.; Drakopoulos, M.; et al. Identifying the Cause of Rupture of Li-Ion Batteries during Thermal Runaway. *Adv. Sci.* **2018**, *5*, 1700369. [\[CrossRef\]](#)
- Kong, L.; Hu, X.; Gui, G.; Su, Y.; Pecht, M. Computed Tomography Analysis of Li-Ion Battery Case Ruptures. *Fire Technol.* **2020**, *56*, 2565–2578. [\[CrossRef\]](#)
- Yao, X.Y.; Kong, L.; Pecht, M.G. Reliability of Cylindrical Li-ion Battery Safety Vents. *IEEE Access* **2020**, *8*, 101859–101866. [\[CrossRef\]](#)
- Golubkov, A.W.; Fuchs, D.; Wagner, J.; Wiltsche, H.; Stangl, C.; Fauler, G.; Voitic, G.; Thaler, A.; Hacker, V. Thermal-runaway experiments on consumer Li-ion batteries with metal-oxide and olivin-type cathodes. *RSC Adv.* **2014**, *4*, 3633–3642. [\[CrossRef\]](#)
- Sturk, D.; Rosell, L.; Blomqvist, P.; Ahlberg Tidblad, A. Analysis of Li-Ion Battery Gases Vented in an Inert Atmosphere Thermal Test Chamber. *Batteries* **2019**, *5*, 61. [\[CrossRef\]](#)
- Essl, C.; Seifert, L.; Rabe, M.; Fuchs, A. Early Detection of Failing Automotive Batteries Using Gas Sensors. *Batteries* **2021**, *7*, 25. [\[CrossRef\]](#)
- Cai, T.; Mohtat, P.; Stefanopoulou, A.G.; Siegel, J.B. Li-ion Battery Fault Detection in Large Packs Using Force and Gas Sensors. *IFAC-PapersOnLine* **2020**, *53*, 12491–12496. [\[CrossRef\]](#)
- Mier, F.A.; Morales, R.; Coultas-McKenney, C.A.; Hargather, M.J.; Ostanek, J. Overcharge and thermal destructive testing of lithium metal oxide and lithium metal phosphate batteries incorporating optical diagnostics. *J. Energy Storage* **2017**, *13*, 378–386. [\[CrossRef\]](#)
- Mier, F.A.; Hargather, M.J.; Ferreira, S.R. Experimental Quantification of Vent Mechanism Flow Parameters in 18650 Format Lithium Ion Batteries. *J. Fluids Eng.* **2019**, *141*, 061403. [\[CrossRef\]](#)
- Hatchard, T.D.; MacNeil, D.D.; Basu, A.; Dahn, J.R. Thermal Model of Cylindrical and Prismatic Lithium-Ion Cells. *J. Electrochem. Soc.* **2001**, *148*, A755. [\[CrossRef\]](#)
- Kim, G.H.; Pesaran, A.; Spotnitz, R. A three-dimensional thermal abuse model for lithium-ion cells. *J. Power Sources* **2007**, *170*, 476–489. [\[CrossRef\]](#)
- Hoelle, S.; Dengler, F.; Zimmermann, S.; Hinrichsen, O. 3D Thermal Simulation of Lithium-Ion Battery Thermal Runaway in Autoclave Calorimetry: Development and Comparison of Modeling Approaches. *J. Electrochem. Soc.* **2023**, *170*, 010509. [\[CrossRef\]](#)

26. Coman, P.T.; Rayman, S.; White, R.E. A lumped model of venting during thermal runaway in a cylindrical Lithium Cobalt Oxide lithium-ion cell. *J. Power Sources* **2016**, *307*, 56–62. [[CrossRef](#)]
27. Coman, P.T.; Mátéfi-Tempfli, S.; Veje, C.T.; White, R.E. Modeling Vaporization, Gas Generation and Venting in Li-Ion Battery Cells with a Dimethyl Carbonate Electrolyte. *J. Electrochem. Soc.* **2017**, *164*, A1858–A1865. [[CrossRef](#)]
28. Huang, W.; Feng, X.; Pan, Y.; Jin, C.; Sun, J.; Yao, J.; Wang, H.; Xu, C.; Jiang, F.; Ouyang, M. Early warning of battery failure based on venting signal. *J. Energy Storage* **2023**, *59*, 106536. [[CrossRef](#)]
29. Ostanek, J.K.; Li, W.; Mukherjee, P.P.; Crompton, K.R.; Hacker, C. Simulating onset and evolution of thermal runaway in Li-ion cells using a coupled thermal and venting model. *Appl. Energy* **2020**, *268*, 114972. [[CrossRef](#)]
30. Wang, G.; Kong, D.; Ping, P.; He, X.; Lv, H.; Zhao, H.; Hong, W. Modeling venting behavior of lithium-ion batteries during thermal runaway propagation by coupling CFD and thermal resistance network. *Appl. Energy* **2023**, *334*, 120660. [[CrossRef](#)]
31. Kim, J.; Mallarapu, A.; Finegan, D.P.; Santhanagopalan, S. Modeling cell venting and gas-phase reactions in 18650 lithium ion batteries during thermal runaway. *J. Power Sources* **2021**, *489*, 229496. [[CrossRef](#)]
32. Kong, D.; Wang, G.; Ping, P.; Wen, J. A coupled conjugate heat transfer and CFD model for the thermal runaway evolution and jet fire of 18650 lithium-ion battery under thermal abuse. *eTransportation* **2022**, *12*, 100157. [[CrossRef](#)]
33. Mao, B.; Zhao, C.; Chen, H.; Wang, Q.; Sun, J. Experimental and modeling analysis of jet flow and fire dynamics of 18650-type lithium-ion battery. *Appl. Energy* **2021**, *281*, 116054. [[CrossRef](#)]
34. Wang, G.; Kong, D.; Ping, P.; Wen, J.; He, X.; Zhao, H.; He, X.; Peng, R.; Zhang, Y.; Dai, X. Revealing particle venting of lithium-ion batteries during thermal runaway: A multi-scale model toward multiphase process. *eTransportation* **2023**, *16*, 100237. [[CrossRef](#)]
35. Wang, J.h.; Jiang, Z.; Mei, M.; Qiu, H.; Wang, Y. Numerical simulation study on two-phase flow of thermal runaway evolution and jet fire of 18650 lithium-ion battery under thermal abuse. *Case Stud. Therm. Eng.* **2024**, *53*, 103726. [[CrossRef](#)]
36. Mishra, D.; Shah, K.; Jain, A. Investigation of the Impact of Flow of Vented Gas on Propagation of Thermal Runaway in a Li-Ion Battery Pack. *J. Electrochem. Soc.* **2021**, *168*, 060555. [[CrossRef](#)]
37. Ping, P.; Wang, Q.; Huang, P.; Li, K.; Sun, J.; Kong, D.; Chen, C. Study of the fire behavior of high-energy lithium-ion batteries with full-scale burning test. *J. Power Sources* **2015**, *285*, 80–89. [[CrossRef](#)]
38. Zou, K.; Chen, X.; Ding, Z.; Gu, J.; Lu, S. Jet behavior of prismatic lithium-ion batteries during thermal runaway. *Appl. Therm. Eng.* **2020**, *179*, 115745. [[CrossRef](#)]
39. Golubkov, A.W.; Scheickl, S.; Planteu, R.; Voitic, G.; Wiltsche, H.; Stangl, C.; Fauler, G.; Thaler, A.; Hacker, V. Thermal runaway of commercial 18650 Li-ion batteries with LFP and NCA cathodes – impact of state of charge and overcharge. *RSC Adv.* **2015**, *5*, 57171–57186. [[CrossRef](#)]
40. Golubkov, A.W.; Planteu, R.; Krohn, P.; Rasch, B.; Brunnsteiner, B.; Thaler, A.; Hacker, V. Thermal runaway of large automotive Li-ion batteries. *RSC Adv.* **2018**, *8*, 40172–40186. [[CrossRef](#)]
41. Zhou, Z.; Zhou, X.; Wang, D.; Li, M.; Wang, B.; Yang, L.; Cao, B. Experimental analysis of lengthwise/transversal thermal characteristics and jet flow of large-format prismatic lithium-ion battery. *Appl. Therm. Eng.* **2021**, *195*, 117244. [[CrossRef](#)]
42. Jia, Z.; Wang, S.; Qin, P.; Li, C.; Song, L.; Cheng, Z.; Jin, K.; Sun, J.; Wang, Q. Comparative investigation of the thermal runaway and gas venting behaviors of large-format LiFePO₄ batteries caused by overcharging and overheating. *J. Energy Storage* **2023**, *61*, 106791. [[CrossRef](#)]
43. Jia, Z.; Min, Y.; Qin, P.; Mei, W.; Meng, X.; Jin, K.; Sun, J.; Wang, Q. Effect of safety valve types on the gas venting behavior and thermal runaway hazard severity of large-format prismatic lithium iron phosphate batteries. *J. Energy Chem.* **2024**, *89*, 195–207. [[CrossRef](#)]
44. Liu, P.; Sun, H.; Qiao, Y.; Sun, S.; Wang, C.; Jin, K.; Mao, B.; Wang, Q. Experimental study on the thermal runaway and fire behavior of LiNi_{0.8}Co_{0.1}Mn_{0.1}O₂ battery in open and confined spaces. *Process. Saf. Environ. Prot.* **2022**, *158*, 711–726. [[CrossRef](#)]
45. Qin, P.; Jia, Z.; Wu, J.; Jin, K.; Duan, Q.; Jiang, L.; Sun, J.; Ding, J.; Shi, C.; Wang, Q. The thermal runaway analysis on LiFePO₄ electrical energy storage packs with different venting areas and void volumes. *Appl. Energy* **2022**, *313*, 118767. [[CrossRef](#)]
46. Wang, S.; Song, L.; Li, C.; Tian, J.; Jin, K.; Duan, Q.; Wang, Q. Experimental study of gas production and flame behavior induced by the thermal runaway of 280 Ah lithium iron phosphate battery. *J. Energy Storage* **2023**, *74*, 109368. [[CrossRef](#)]
47. Li, J.; Tong, B.; Gao, P.; Cheng, Z.; Cao, M.; Mei, W.; Qin, P.; Sun, J.; Wang, Q. A novel method to determine the multi-phase ejection parameters of high-density battery thermal runaway. *J. Power Sources* **2024**, *592*, 233905. [[CrossRef](#)]
48. Wang, Y.; Song, Z.; Li, Y.; Li, C.; Ren, D.; Feng, X.; Wang, H.; Lu, L. Experimental investigation of the thermal propagation, emission identification, and venting-flow characteristics of a Li(Ni_{0.8}Co_{0.1}Mn_{0.1})O₂ battery module. *Case Stud. Therm. Eng.* **2023**, *49*, 103360. [[CrossRef](#)]
49. García, A.; Zhao, P.; Monsalve-Serrano, J.; Villalta, D.; Martinez-Boggio, S. Optical diagnostics of the venting spray and combustion behaviour during Li-ion battery thermal runaway induced by ramp heating. *Appl. Therm. Eng.* **2023**, *218*, 119308. [[CrossRef](#)]
50. García, A.; Monsalve-Serrano, J.; Sari, R.L.; Martinez-Boggio, S. Influence of environmental conditions in the battery thermal runaway process of different chemistries: Thermodynamic and optical assessment. *Int. J. Heat Mass Transf.* **2022**, *184*, 122381. [[CrossRef](#)]
51. García, A.; Monsalve-Serrano, J.; Lago Sari, R.; Martinez-Boggio, S. An optical investigation of thermal runaway phenomenon under thermal abuse conditions. *Energy Convers. Manag.* **2021**, *246*, 114663. [[CrossRef](#)]
52. Leung, J.C. Venting of runaway reactions with gas generation. *AIChE J.* **1992**, *38*, 723–732. [[CrossRef](#)]

53. Finegan, D.P.; Billman, J.; Darst, J.; Hughes, P.; Trillo, J.; Sharp, M.; Benson, A.; Pham, M.; Kesuma, I.; Buckwell, M.; et al. The battery failure databank: Insights from an open-access database of thermal runaway behaviors of Li-ion cells and a resource for benchmarking risks. *J. Power Sources* **2024**, *597*, 234106. [[CrossRef](#)]
54. Mao, B.; Fear, C.; Chen, H.; Zhou, H.; Zhao, C.; Mukherjee, P.P.; Sun, J.; Wang, Q. Experimental and modeling investigation on the gas generation dynamics of lithium-ion batteries during thermal runaway. *eTransportation* **2023**, *15*, 100212. [[CrossRef](#)]
55. Zhao, C.; Sun, J.; Wang, Q. Thermal runaway hazards investigation on 18650 lithium-ion battery using extended volume accelerating rate calorimeter. *J. Energy Storage* **2020**, *28*, 101232. [[CrossRef](#)]
56. Sharp, M.; Darst, J.J.; Hughes, P.; Billman, J.; Pham, M.; Petrushenko, D.; Heenan, T.M.M.; Jervis, R.; Owen, R.; Patel, D.; et al. Thermal Runaway of Li-Ion Cells: How Internal Dynamics, Mass Ejection, and Heat Vary with Cell Geometry and Abuse Type. *J. Electrochem. Soc.* **2022**, *169*, 020526. [[CrossRef](#)]
57. Essl, C.; Golubkov, A.W.; Fuchs, A. Comparing Different Thermal Runaway Triggers for Two Automotive Lithium-Ion Battery Cell Types. *J. Electrochem. Soc.* **2020**, *167*, 130542. [[CrossRef](#)]
58. Essl, C.; Golubkov, A.W.; Fuchs, A. Influence of Aging on the Failing Behavior of Automotive Lithium-Ion Batteries. *Batteries* **2021**, *7*, 23. [[CrossRef](#)]
59. Sturm, J.; Rheinfeld, A.; Zilberman, I.; Spingler, F.B.; Kosch, S.; Frie, F.; Jossen, A. Modeling and simulation of inhomogeneities in a 18650 nickel-rich, silicon-graphite lithium-ion cell during fast charging. *J. Power Sources* **2019**, *412*, 204–223. [[CrossRef](#)]
60. Lain.; Brandon.; Kendrick. Design Strategies for High Power vs. High Energy Lithium Ion Cells. *Batteries* **2019**, *5*, 64. [[CrossRef](#)]
61. Feng, X.; Ren, D.; He, X.; Ouyang, M. Mitigating Thermal Runaway of Lithium-Ion Batteries. *Joule* **2020**, *4*, 743–770. [[CrossRef](#)]
62. Ohneseit, S.; Finster, P.; Floras, C.; Lubenau, N.; Uhlmann, N.; Seifert, H.J.; Ziebert, C. Thermal and Mechanical Safety Assessment of Type 21700 Lithium-Ion Batteries with NMC, NCA and LFP Cathodes—Investigation of Cell Abuse by Means of Accelerating Rate Calorimetry (ARC). *Batteries* **2023**, *9*, 237. [[CrossRef](#)]
63. National Renewable Energy Laboratory, Battery Failure Databank. Available online: <https://www.nrel.gov/transportation/battery-failure.html> (accessed on 11 March 2024).

Disclaimer/Publisher’s Note: The statements, opinions and data contained in all publications are solely those of the individual author(s) and contributor(s) and not of MDPI and/or the editor(s). MDPI and/or the editor(s) disclaim responsibility for any injury to people or property resulting from any ideas, methods, instructions or products referred to in the content.